ANNALS OF GEOPHYSICS, 66, 2, SE214, 2023; doi:10.4401/ag-8874
OPEN ACCESS

Rayleigh phase velocity and azimuthal anisotropy from ambient noise data in the Sanjiang lateral collision zone in the SE margin of the Tibetan plateau

Jianhui Tian[1,2], Yuan Gao[*,2] and Ying Li[3,2]

(1) Institute of Geophysics, China Earthquake Administration, Beijing 100081, China
(2) Key Laboratory of Earthquake Prediction, Institute of Earthquake Forecasting, China Earthquake Administration, Beijing 100036, China
(3) School of Earth and Space Sciences, University of Science and Technology of China, Hefei, 230026, China

Article history: received June 30, 2022; accepted May 29, 2023

Abstract

The Sanjiang lateral collision zone in the SE margin of the Tibetan Plateau is located at the east edge of the junction of the Eurasian and Indian plates. Using the continuous seismic waveforms recorded by 146 temporary and 21 permanent seismic stations in the study area, we obtain Rayleigh wave phase velocity and azimuthal anisotropy for periods 2 s to 40 s from the surface wave direct tomography method. This direct tomography method can obtain finer high-resolution results than the traditional surface wave tomography. Our results show that the low-velocity anomalies are found beneath the Lijiang-Xiaojinhe fault (LXF), Red River fault (RRF), Chuxiong fault and Tengchong volcanoes, the high-velocity anomalies are in the region of Weixi and Panzhihua at periods 5 ~ 8 s. The fast velocity directions mainly align N-S. At periods 10 ~ 15 s, the distributions of low-velocity anomalies are consistent with the strikes of LXF and RRF. At periods 20 ~ 35 s, the high- and low-velocity anomalies are bounded by the RRF, which may imply the fault is divided by the thick crust (indicated by low-velocity anomalies) and the thin crust with shallow mantle (indicated by high-velocity anomalies). The fast velocity directions at the periods 10 ~ 35 s rotate clockwise from north to south of the study area. The intensity of anisotropy in the low-velocity zone is stronger than that in the high-velocity zone, and the intensity in the north of the study area is stronger than that in the south. Results indicate the source of anisotropy may be different in each subzone.

Keywords: SE margin of the Tibetan Plateau; Sanjiang lateral collision zone; Rayleigh wave; Phase velocity; Azimuthal anisotropy

1. Introduction

The continuous collision and extrusion of the Eurasian and Indian plates have facilitated the eastward migration of the Tibetan Plateau material, forming the characteristics of high altitude and thick crust [Yin and Harrison, 2000]. However, the eastward migration encounters the barrier of the Sichuan Basin, which caused diversion of the plateau material in the northeast and southeast directions. Within this context, the SE margin of the Tibetan Plateau serves as the channel of the plateau material flowing in the direction of NW-SE to nearly N-S [Royden et al., 2008], resulting in the clockwise rotation of surface movement. In recent years, GPS observations have provided clear evidence of this clockwise rotational motion around the eastern Himalayan syntaxis, with significant crustal strains primarily concentrated in the faults [Jin et al., 2019; Wang and Shen, 2020; Zhao et al., 2015].

Located in the SE margin of the Tibetan Plateau and the southwestern of the Sichuan-Yunnan rhombic block (Figure 1), the Sanjiang lateral collision zone is considered to be the intersection of the Tethys tectonic belt and the western Pacific tectonic belt. The region has experienced two significant stages of the Tethys accretionary orogeny and the India-Eurasia plate intercontinental collision orogeny, resulting in complex tectonics, strong deformation and frequent seismic activity in the study area [Pan, 1991; Liu et al., 1993; Zhong and Ding, 1993]. The study area is not only distributed Chuxiong basin (green shadow in Figure 1a) and the inner zone of the Emeishan large igneous province (ELIP) (pink dashed lines in Figure 1), but also active Tengchong volcanoes (TCV) (red triangle in Figure 1) and many deep faults, such as Lancangjiang fault (LCJF), Nujiang fault (NJF), Chenghai fault (CHF), Lijiang-Xiaojinhe fault (LXF), Jinhe-Qinghe fault (JQF), Longling-Ruili fault (LRF) and Chuxiong fault (CXF) (Figure 1). These complex faults divide the study area into different tectonic units, namely the Tengchong block (TCB), Baoshan block (BSB), the Indochina block (ICB), the Western Sichuan sub-block (WSB) and the Central Yunnan sub-block (CYB) from west to east. The NW-trending RRF is a giant strike-slip fault that cuts through the ICB and the South China block. It serves as the western boundary of the Sichuan-Yunnan rhombic block and plays a key role in the eastward extrusion of material from the SE margin of the Tibetan Plateau. Therefore, it is necessary to study the velocity structure and azimuthal anisotropy of the Sanjiang lateral collision zone as a key place for the lateral extrusion and escape of the Tibetan Plateau material.

Since the 1980s, the deep seismic sounding [Bai and Wang, 2003], magnetotelluric tomography [Bai et al., 2010], various scales of body-wave tomography [Lei et al., 2009, 2014; Yang et al., 2014], surface-wave tomography [Li et al., 2014; Qiao et al., 2018; Wang and Gao, 2014; Wang et al., 2015; Yao et al., 2008, 2010; Zhang et al., 2020], receiver functions studies [Cai et al., 2016; Sun et al., 2012; Zhang and Gao, 2019] and shear-wave splitting [Chang et al., 2015; Gao and Wu, 2008; Gao et al., 2011, 2019, 2020; Lev et al., 2006; Shi et al., 2012; Wang et al., 2007; Zhang and Gao, 2017] have been carried out in the study area. These available research data indicated that the structure of the crust and upper mantle is laterally heterogeneous and dominated by low-velocity, low resistivity, high electrical conductivity, high heat flow, low Q value and strong anisotropy [Bai et al., 2010; Cai et al., 2016; Hu et al., 2000; Sun et al., 2016; Zhang et al., 2020; Zhao et al., 2013]. It is widely accepted that the low-velocity layers exist in the middle-lower crust. Some authors supported the middle-lower crustal flow model and suggested that there may be a channel for material flowing in the Yunnan province, China [Bao et al., 2015; Li et al., 2016; Royden et al., 1997; Wu et al., 2016]. However, based on the heterogeneity of the crustal low-velocity layer, some authors suggested that the lower crustal flow in the SE margin of the Tibetan Plateau is confined to local areas by faults and tectonic boundaries [Chen et al., 2014; Chen et al., 2016; Wang et al., 2010; Yao et al., 2008]. Recently, Zhang et al. [2020] proposed that the SE margin of the Tibetan Plateau is experiencing three different tectonic modes simultaneously. Although the above-mentioned results from different methods are comparable and have a deep understanding of the crust-mantle structure in the study area, the lateral and vertical velocity distributions show important differences mainly due to the large scale and resolution limitations.

The surface waves propagate in a stratified medium, which are characterized by the dispersion, and the surface wave dispersion is sensitive to the S wave velocity of the medium. Furthermore, the surface wave data contains a wealth of crust-mantle structure information beneath the propagation path. So, surface wave tomography using dispersion data to obtain isotropic and anisotropic models is a very efficient approach for studying regional tectonics and deformation as well as probing high-resolution crustal structures [Yao et al., 2023]. Generally, traditional surface wave tomography based on dispersion data usually has two steps. Firstly, 2D phase or group velocity maps are inverted. Then, a 1D S wave velocity model is derived at each grid point based on the pure path dispersion of the grid point. Finally, these 1D models are combined to construct a 3D S wave velocity model [Yao et al., 2023]. However, the conventional tomography method faces challenges when there are limited paths available for constructing reliable

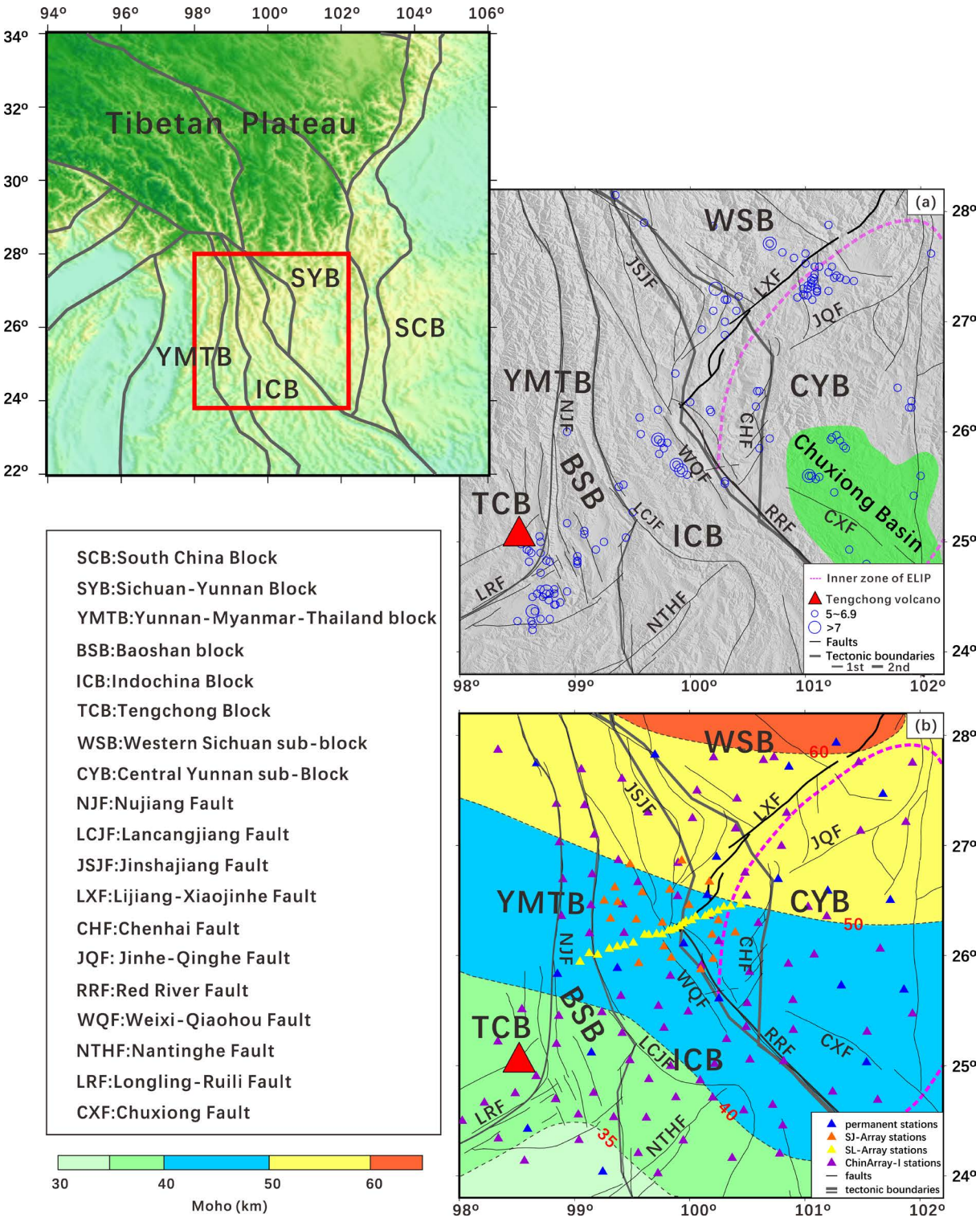

Figure 1. Tectonic background and seismic station distribution in the study area. (a) Tectonic background of the study area. The red triangle represents the location of the Tengchong volcanic region. The pink dashed lines outline the inner zone of the ELIP [Xu et al., 2004]. The blue circles represent earthquakes of $M > 5.0$ from 1970 to 2021 (https://data.earthquake.cn/). The major faults and tectonic boundaries are depicted with solid black and gray lines, respectively. Some important faults and blocks are indicated with their initials (in black), whose meaning is shown in the rectangular box on the left. The inset in the top left shows the location of the study area. (b) Distribution of stations. The triangles of different colors represent different types of stations, whose meaning is shown at the bottom right corner. The background color is the depth of Moho modified from Zhu et al. [2021].

2D phase or group velocity maps for certain periods. Consequently, data from these periods cannot be effectively utilized in the two-step surface wave tomography [Luo et al., 2019; Yao et al., 2010; Yao et al., 2023]. To address this limitation, recently advancements have been made in surface wave tomography. Fang et al. [2015] and Zhang et al. [2019] developed the direct surface wave tomography method based on surface wave dispersion traveltimes, that is one-step method. This method allows for the utilization of dispersion traveltimes from all periods in surface wave tomography, enhancing data coverage density and improving resolution.

In our research works, in addition to the regional permanent stations and the ChinArray Phase I (ChinArray-I) stations used in previous studies, we also benefited from the two temporary seismic arrays (SJ-array and SL-array) set up by the Institute of Earthquake Forecasting, China Earthquake Administration in the Sanjiang lateral collision zone, which provides more detailed velocity structure and azimuthal anisotropy in the study area. We first used the direct surface wave tomography method by the observed continuous seismic waveforms of temporary seismic arrays and regional permanent stations to obtain the 3D S wave velocity and azimuthal anisotropy in the study area, and then perform a forward calculation of the phase velocity and azimuthal anisotropy for each grid point at different periods based on our 3D S wave velocity. The 3D S wave velocity and azimuthal anisotropy will be discussed in detail later in another study. In this paper, the phase velocity and azimuthal anisotropy obtained by further calculation are mainly discussed, and the phase velocity results in this paper are compared with those obtained by the previous conventional method.

2. Data and Method

2.1 Data resources and Dispersion processing

The temporary linear arrays (SL-Array) and areal arrays (SJ-Array) were set up in the study area by the Institute of Earthquake Forecasting, China Earthquake Administration in October 2016 and October 2018, respectively. The seismograph has a period of 120 s. In this study, we use the continuous seismic waveforms recorded by SL-Array from November 2016 to December 2018, SJ-Array from October 2018 to December 2020, the stations of ChinArray-I from October 2011 to December 2013 and Yunnan regional permanent stations from December 2012 to July 2020 (Figure 1b). The even and dense distribution of these stations ensures a good resolution for ambient noise tomography.

The waveforms were first down-sampled form 100 Hz to 5 Hz and then used to compute interstation ambient noise cross-correlation functions (CFs) mainly following the processing schemes of Bensen et al. [2007], including removing instrument response, removing mean and trend, band-pass filtering (2 ~ 50 s), spectral whitening, and temporal normalization of the waveform data. Finally, we calculated the CFs of all station pairs. Figure 2 shows

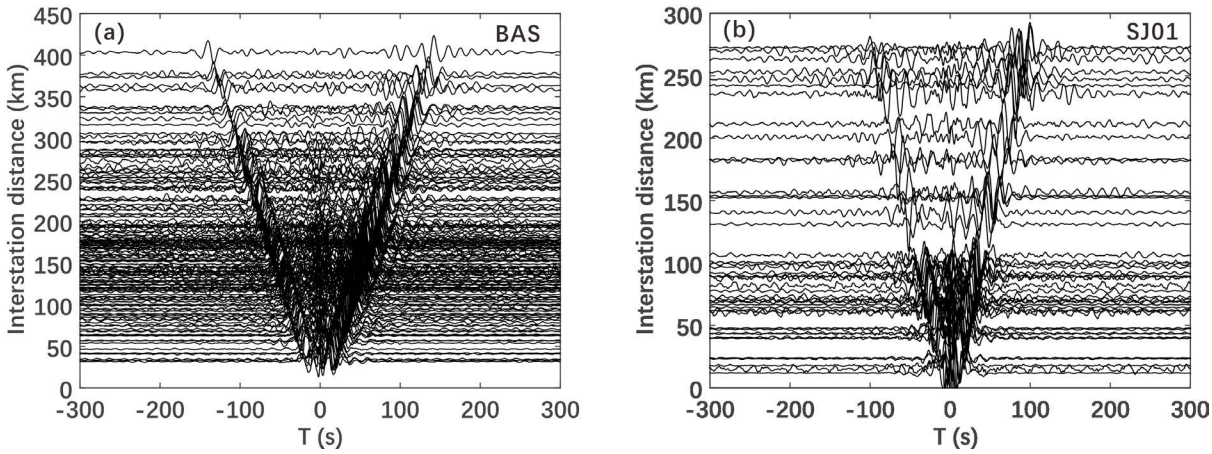

Figure 2. Examples of CFs at periods of 2 s to 40 s as a functions of interstation distance (a) CFs between permanent station BAS and all other stations. (b) CFs between station SJ01 and permanent stations, the remaining SJ-arrays.

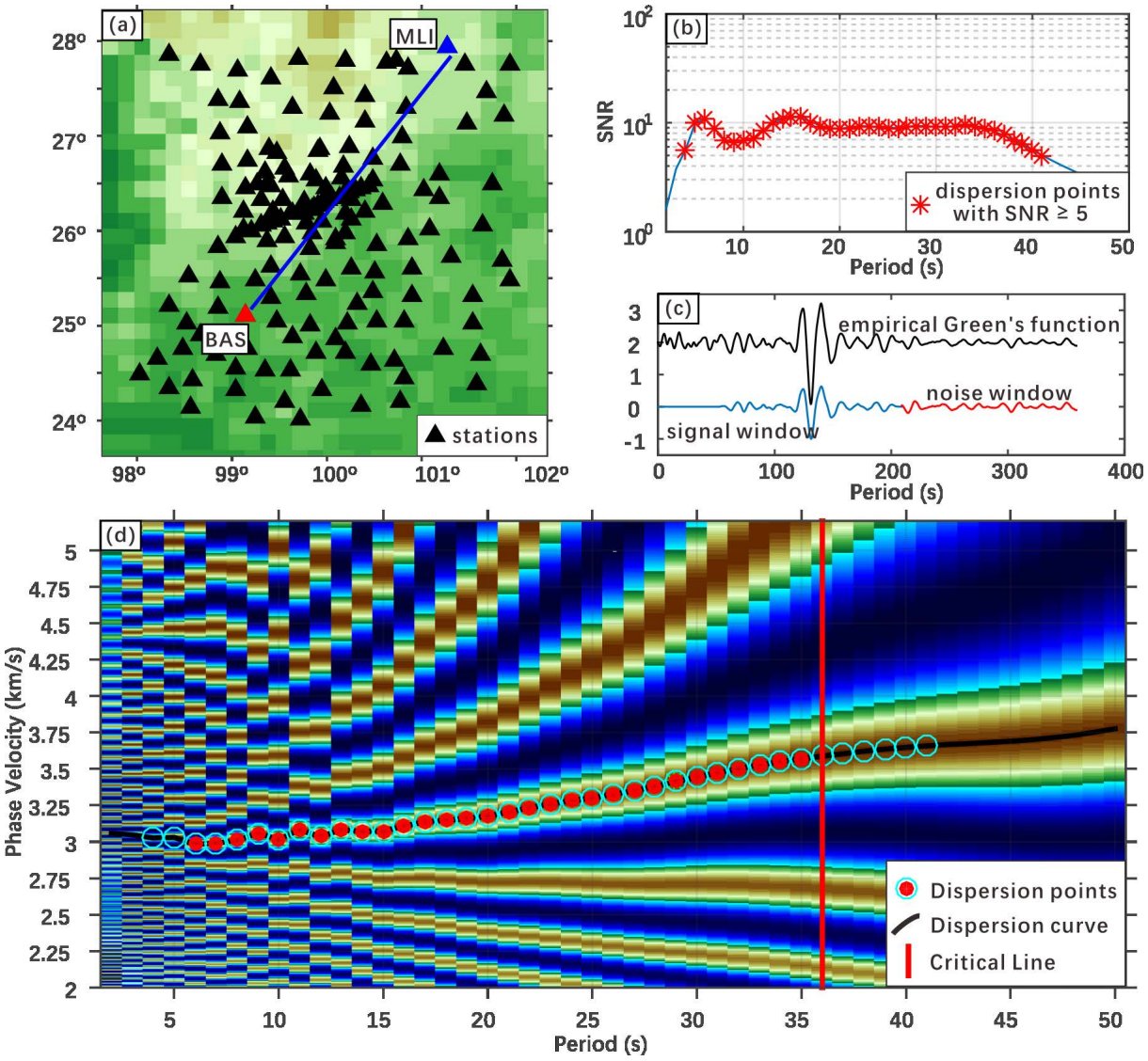

Figure 3. Example of phase velocity dispersion curve measurements at BAS-MLI station. (a) Station pair location map. (b) Magnitude of signal-to-noise ratio corresponding to different periods. (c) The empirical Green function and the waveform after adding the time window. (d) Phase velocity dispersion curve measurement plot.

the CFs examples of the station BAS and all other stations (Figure 2a), as well as the station SJ01 and permanent stations and the remaining SJ-arrays (Figure 2b). A clear Rayleigh wave signal can be observed from the Figure 2.

The empirical Green functions were then obtained from the time derivatives of the CFs [Yao et al., 2006]. Under the assumption of far-field surface wave propagation, we extracted the phase velocity dispersion curve based on the image analysis method [Yao et al., 2006]. Figure 3 shows an example of phase velocity dispersion curve measurements at BAS-MLI station. The phase velocity measurements were picked based on the interstation distance and the signal-to-noise ratio of the empirical Green functions. We only retained phase velocity measurements with the signal-to-noise ratio equal to or greater than 5 and interstation distances greater than 2.5 times the wavelength. We finally obtained approximately 5228 phase velocity dispersion curves at the periods 2 s to 40 s. Figure 4 shows number of ray paths, average phase velocity and standard deviation of Rayleigh waves at all periods. We notice that the path number is more than 2000 at most periods and can reach above 3000 at intermediate periods. Figure 5 show the distributions of ray path and ray density at selected periods. We calculated the ray density for grid $0.1° \times 0.1°$ and $0.2° \times 0.2°$, respectively. It can be seen that the paths are distributed evenly in the study area, which ensures the reliability of the inversion results. Figure 6 shows the sensitivity analysis of the Rayleigh wave phase velocity to the S wave velocity structure at different periods (Figure 6b). The initial velocity model (Figure 6a) derived from the 1D velocity model of the SE margin of the Tibetan Plateau [Zhang et al., 2020]. The sensitivity map shows that

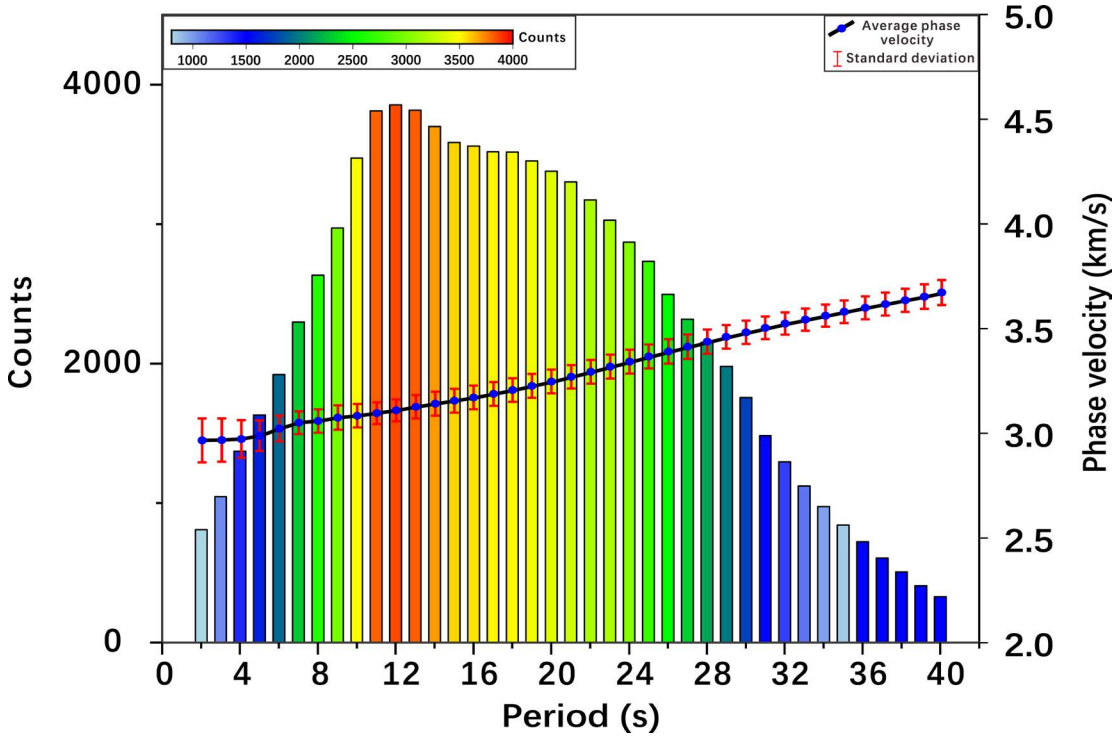

Figure 4. Number of ray paths, average phase velocity and standard deviation of Rayleigh waves at periods 2 ~ 40 s. The histogram is the number of Rayleigh wave ray paths at periods 2 ~ 40 s. The dot-line map is average phase velocity and standard deviation at periods 2 ~ 40 s.

the Rayleigh waves at period 8 s are mainly sensitive to the S wave velocity above 10 km in the upper crust, and its sensitive depth reaches 15 ~ 35 km at the period 25 s, which represents the middle-lower crust in the study area. The Rayleigh wave sensitive depth is greater than 40 km at the period 35 s (Figure 6b).

2.2 The direct inversion method for azimuthal anisotropy

In our research, we used the direct inversion method proposed by Liu et al. [2019]. Firstly, this method assumes the azimuthally anisotropic phase velocity variations are typically several percent in amplitude, which are much smaller than the isotropic phase velocity variations [Liu et al., 2019; Zhang et al., 2022]. Secondly, the traditional surface wave tomography method is based on the individual inversion for the S wave velocity model at each grid point and there is no constraint between adjacent grid points [Liu et al., 2019; Yao et al., 2023; Zhang et al., 2022], while the direct inversion method can directly invert for the 3D S wave velocity structure with lateral and vertical model smoothness constraints [Liu et al., 2019; Zhang et al., 2022]. Finally, the direct inversion method utilizes dispersion data from all periods, enhancing data utilization and improving resolution and accuracy [Liu et al., 2019; Fang et al., 2015; Yao et al., 2023]. The Rayleigh wave traveltimes were calculated by fast-marching ray tracing method proposed by Rawlinson and Sambridge [2005]. The fast-marching ray tracing method is a grid based numerical scheme for tracking the evolution of monotonically advancing interfaces via finite-difference solution of the eikonal equation and distinguishes itself by combining both unconditional stability and rapid computation [Rawlinson and Sambridge, 2004]. Considering the possible tradeoff between the isotropic S wave velocity and the azimuthal anisotropy parameter in the inversion [Yao et al., 2023], we usually use a two-stage method for inversion, including (1) the 3D S wave velocity model is inverted directly from Rayleigh wave traveltimes [Fang et al., 2015]; (2) the reliable S wave velocity model obtained in the first step is considered as an initial model in the second step to invert for both 3D S wave azimuthal anisotropy and additional S wave velocity perturbations [Liu et al., 2019; Zhang et al., 2022]. In this paper, the Rayleigh wave phase velocity and azimuthal anisotropy for each grid point at different periods were perform a forward calculation based on our inversion results obtained in the second step. More details about this recently developed direct inversion method can be found in Liu et al. [2019].

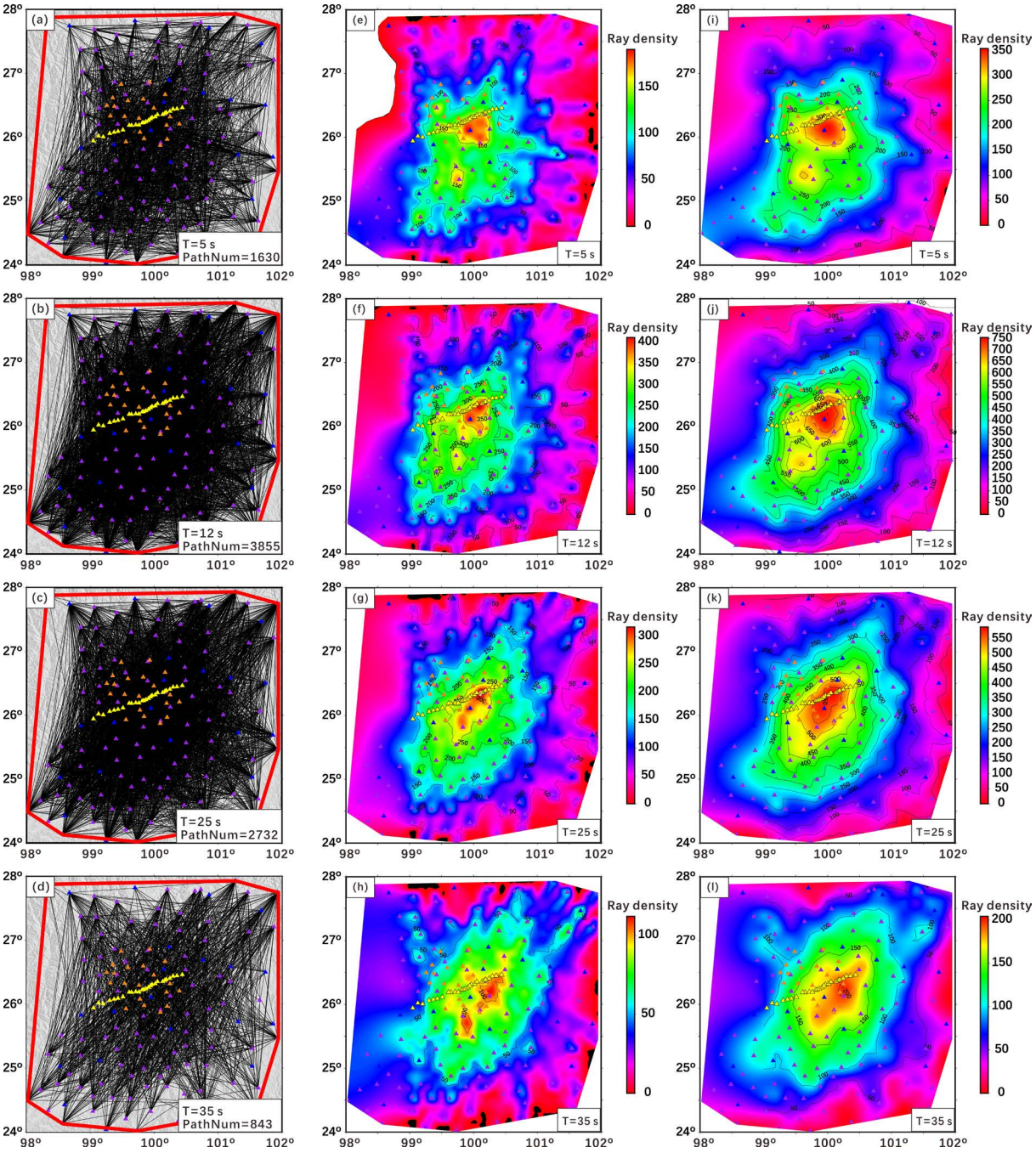

Figure 5. The path coverage and ray density at periods 5, 12, 25 and 35 s. (a)-(d) The path coverage at periods 5, 12, 25 and 35 s, respectively. The black lines are the ray paths. "T" is the period, and "PathNum" is the path number at the corresponding period. The red solid polygon shows that the area has good ray coverage. (e)-(h) The ray density at periods 5, 12, 25 and 35 s with grid size of 0.1° × 0.1°. (i)-(l) The ray density at periods 5, 12, 25 and 35 s with grid size of 0.2° × 0.2°. The triangles are the stations, its meaning is consistent with Figure 1b.

2.3 Checkerboard tests

We conducted checkerboard tests to analyze the resolution of the Rayleigh wave phase velocity and azimuthal anisotropy model. To analyze the recovery ability more comprehensively, we tested checkerboard sizes of 0.75° × 0.75° and 0.6° × 0.6° patterns for anisotropy, 0.5° × 0.5° and 0.4° × 0.4° patterns for isotropy. The isotropic velocity perturbation is ± 5%, and the magnitude of azimuthal anisotropy is 4%. The study area was meshed with a grid size of 0.1° × 0.1° in the horizontal direction and of 3 km from 0 to 15 km, 5 km from 15 to 50 km in the

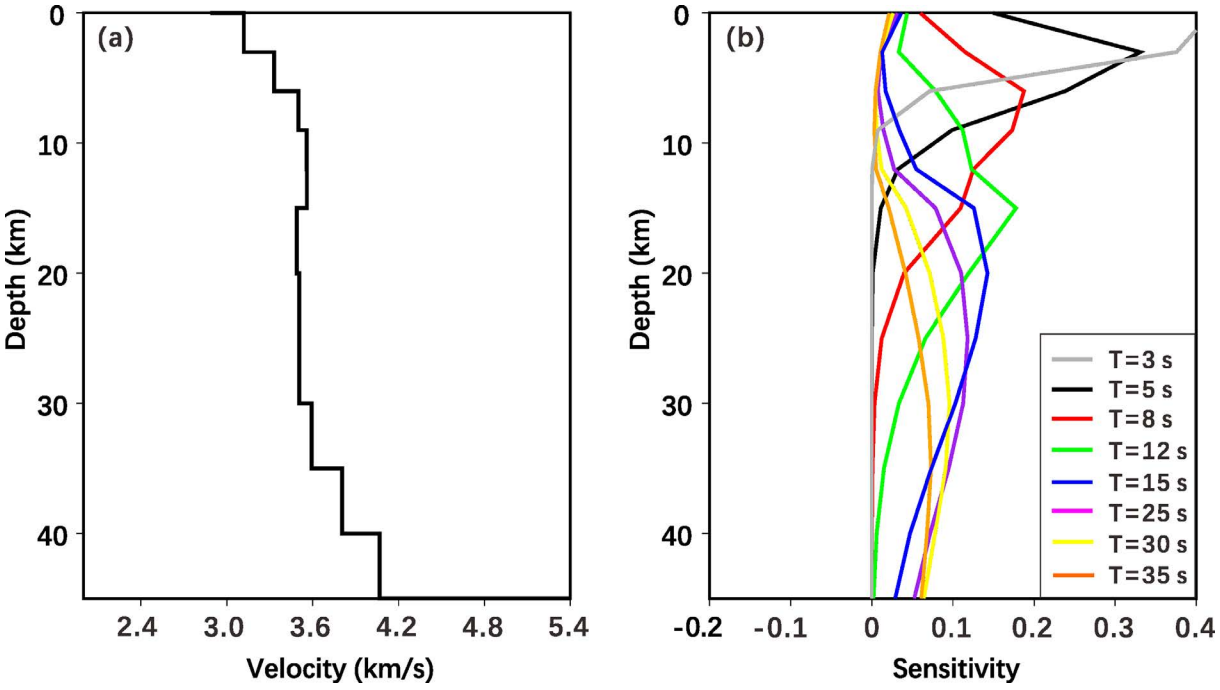

Figure 6. Velocity model used for the inversion and velocity-sensitive kernel analysis. (a) Initial velocity model used for the inversion [Zhang et al., 2020]. (b) Depth sensitivity kernels at periods of 3, 5, 8, 12, 15, 25, 30 and 35 s for the Rayleigh wave fundamental phase velocity calculated using the model in (a).

vertical direction. In the direct inversion, the optimal isotropic weighting factor λ=40 and the optimal anisotropic weighting factor λ=30 determined by L-curve analysis (Figure 7) were used as the input, and the maximum number of iterations for isotropy and anisotropy were set to 15 and 5, respectively. The L-curve analysis, depicted in Figure 7, played a crucial role in determining the optimal weighting factors. By evaluating the trade-off between the misfit

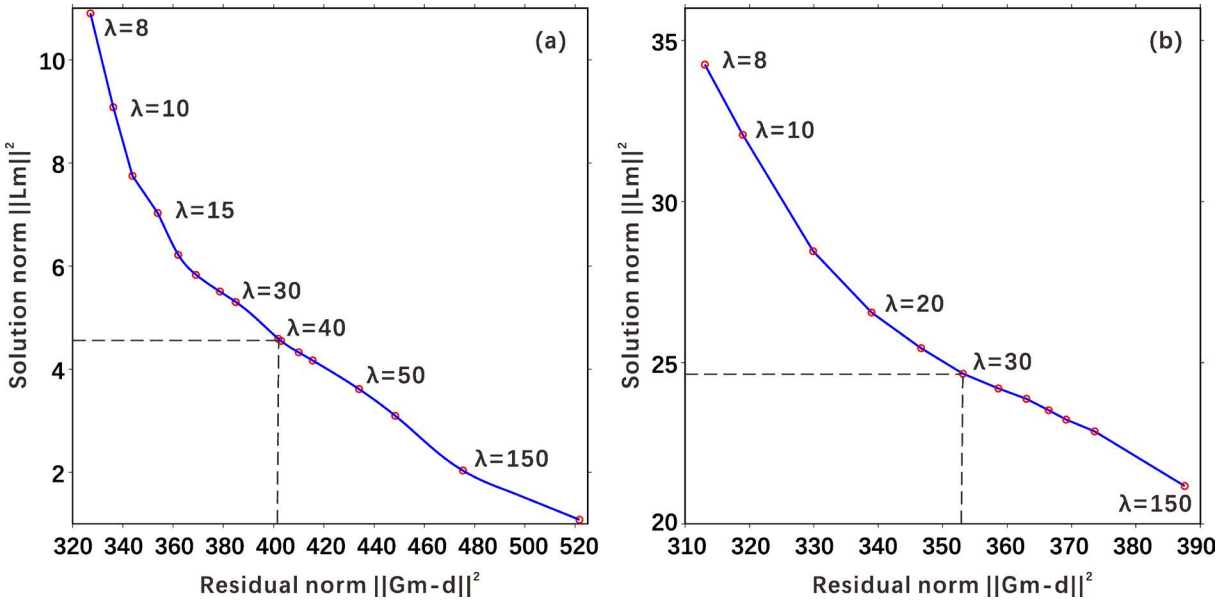

Figure 7. L-curve analysis for the direct inversion. (a) L-curve analysis for isotropic inversion. (b) L-curve analysis for anisotropic inversion. The horizontal axis is the data residual term, and the vertical axis is the model regularization term. The parameter λ is the weighting factor, and the point indicated by the black dashed line is the optimal value of λ.

and model smoothness, the L-curve analysis helped select appropriate values for λ, ensuring a balance between data fit and model complexity.

Figure 8 shows the recovery results of phase velocity and azimuthal anisotropy with different anomaly sizes at 10 s, 20 s and 30 s, respectively. The phase velocity anomalies with size of 0.5° × 0.5° can be well recovered

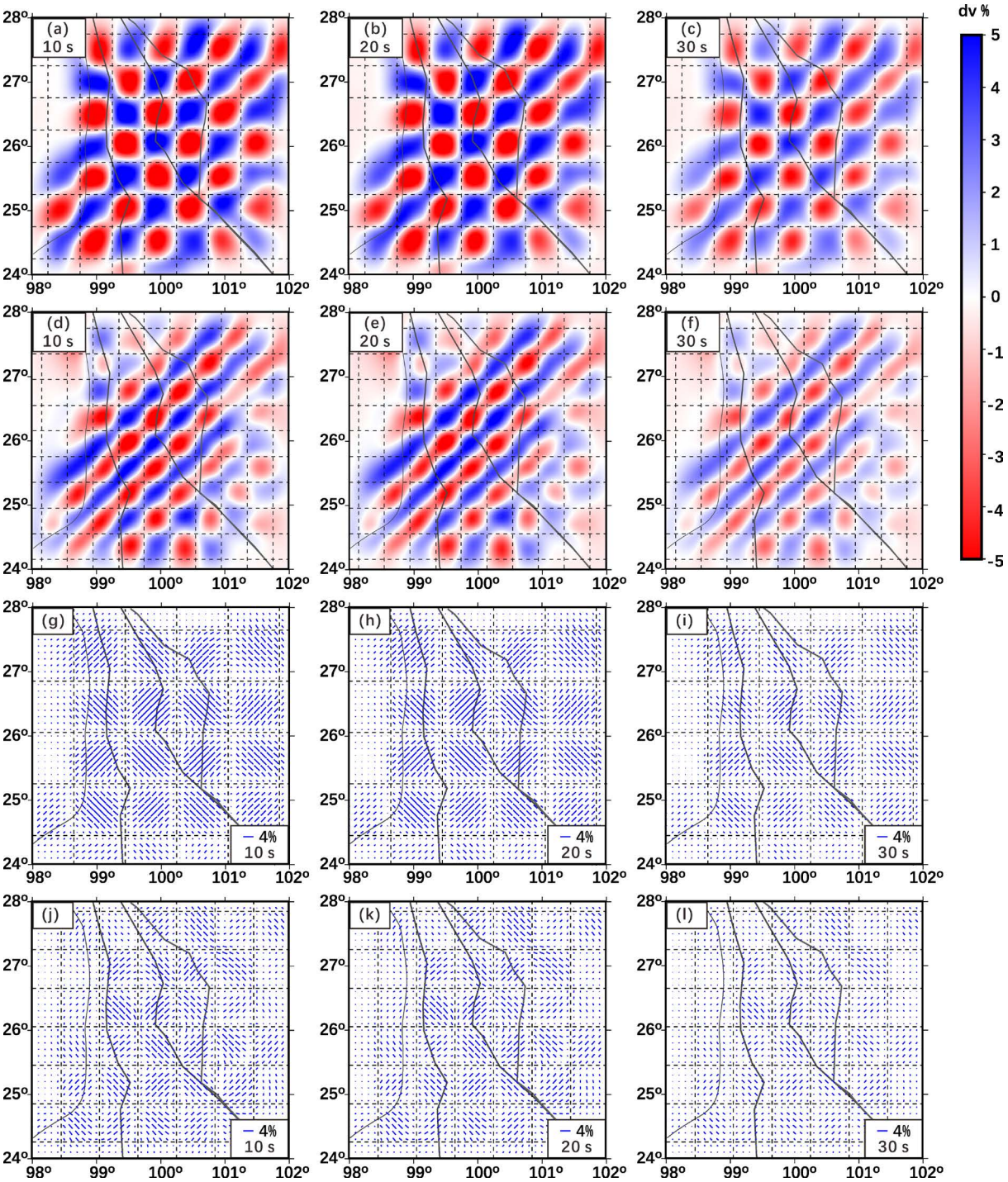

Figure 8. Rayleigh wave phase velocity and azimuthal anisotropy recovery results for periods 10 s, 20 s and 30 s with different anomaly sizes. (a)-(c) and (d)-(f) are the phase velocity recovery results with anomalies sizes of 0.5° × 0.5° and 0.4° × 0.4° for periods 10 s, 20 s and 30 s, respectively. (g)-(i) and (j)-(l) are the azimuthal anisotropy recovery results with anomalies sizes of 0.75° × 0.75° and 0.6° × 0.6° for periods 10 s, 20 s and 30 s, respectively. The velocity anomaly is ± 5% and the magnitude of azimuthal anisotropy is 4%. The dashed black lines in (a)-(l) show the boundary of the true isotropic and anisotropic checkerboard patterns. The gray lines are the tectonic boundaries.

(Figures 8a ~ 8c). For the azimuthal anisotropy, the intensity and direction except the edge region can be well recovered when the anomaly with size of 0.75° × 0.75° (Figures 8g ~ 8i). When the anomaly with size of 0.6° × 0.6°, the recoverable region gradually decreases as the period increases, and only the region near the dense temporary array can be recovered at period of 30 s (Figure 8l). The results of the checkerboard tests emphasize the strong correlation between resolution ability and ray path and density distribution. It can be seen the ray paths before the period of 25 s have better coverage in most of the study area from Figure 5, while after the period of 25 s, ray paths are more concentrated near the dense temporary arrays.

3. Results

The Rayleigh wave phase velocity and azimuthal anisotropy model at selected periods are shown in Figure 9. At short periods (5 ~ 10 s), the phase velocity map shows great lateral heterogeneity. The low-velocity zone extends southwestward along LXF into the ICB and TCB. Two high-velocity zones are presented on both sides of the low-velocity zone, distributed in Panzhihua region within the Sichuan-Yunnan block and Weixi region on the edge of Sanjiang lateral collision zone. In addition, there are small-scale high-velocity anomaly between the south side of the LRF and the west side of the Shidian region. The high-velocity anomaly around the LCJF arc structure is consistent with the strike of the fault. The fast velocity directions mainly align N-S in most of the study regions,

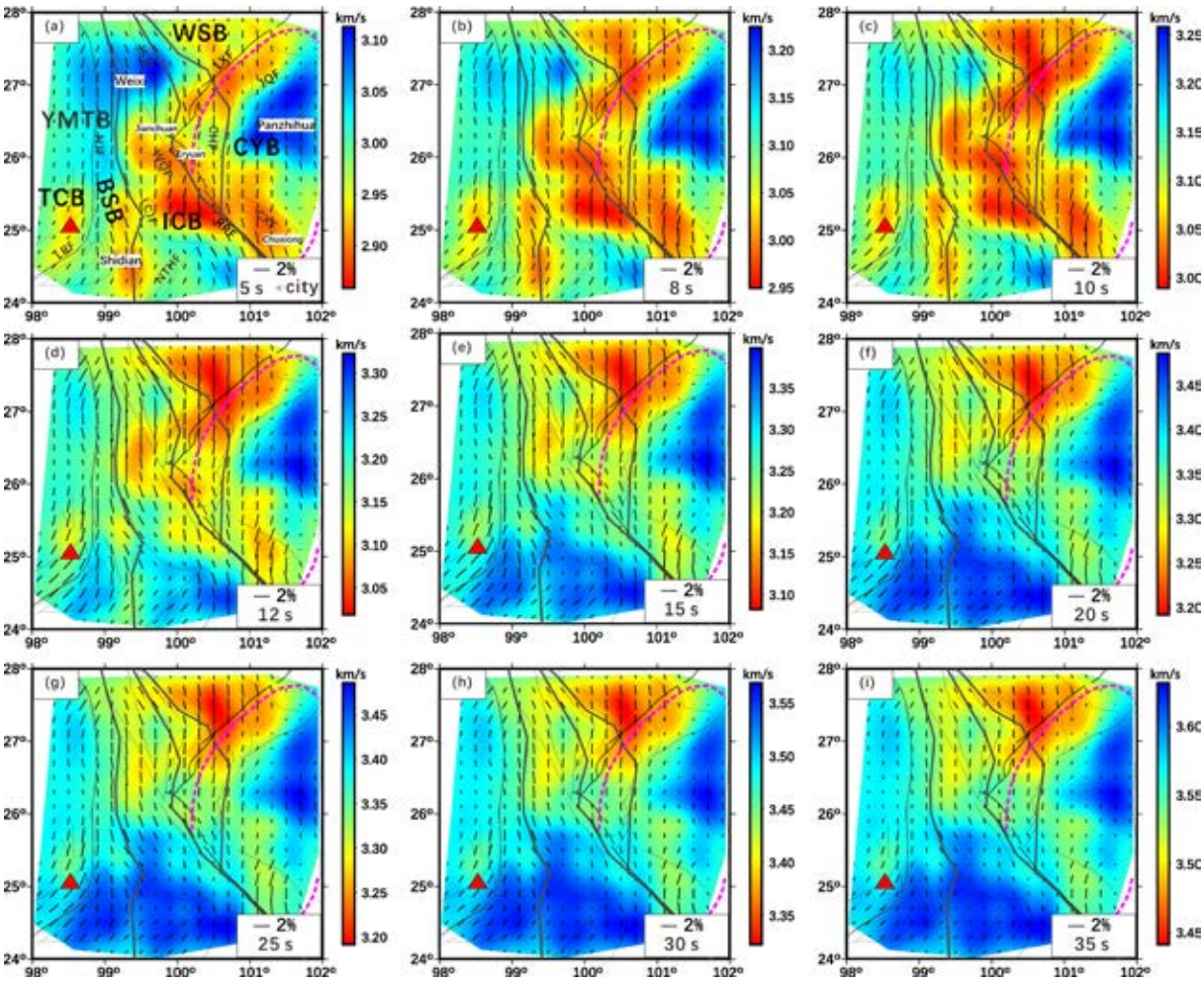

Figure 9. Results of the Rayleigh wave phase velocity and azimuthal anisotropy at selected periods. The background color is the Rayleigh wave phase velocity, red and blue colors denote the low and high velocity anomalies, respectively, whose scale is shown at the right side. The azimuth and length of the black lines denote the direction and the intensity of azimuthal anisotropy, respectively. Other symbols and abbreviations are consistent with Figure 1.

except for some NNW-SSE and ENE-WSW trending in the TCV and Shidian region. Stronger anisotropy is found in the TCV and south of the northwestern end of the RRF.

At periods 12 ~ 20 s (Figures 9d ~ 9f), several notable changes can be observed. The low-velocity zone on the north side of LXF gradually move westward. The low-velocity zone in the southern side of TCV and the Shidian region gradually becomes high-velocity. As the period increases, the range of the low-velocity anomaly on the southwestern side of the study area gradually increases. The fast velocity directions are consistent with the strike of the faults in the west side of RRF, while the directions are nearly N-S in the east. In addition, the anisotropy direction shows ENE-WSW in the vicinity of Eryuan and Jianchuan region, which are located in the intersection area of different faults, indicating that the deformation of the intersection area is more complex. Compared with the maps of short period, the intensity of anisotropy in the low-velocity zone is enhanced, especially near the LXF.

At periods 25 ~ 35 s (Figures 9g ~ 9i), the velocity structure is essentially restricted by the RRF, which is a high-velocity in the southwest and a low-velocity in the northeast. The results of the receiver functions show that the depth of the Moho in the northeast of the study area is more than 50 km, and the southwest is 35.1 ~ 38.3 km [Figure 1b, Sun et al., 2012; Wang et al., 2017]. Therefore, the velocity distribution in this period corresponds to the characteristics of crustal thickness. The fast velocity directions are NNW-SSE in the west side of CHF, which is consistent with the strike of RRF, indicating that the RRF has a strong influence on anisotropy. The intensity of anisotropy also shows great lateral heterogeneity. The anisotropy intensity in the west of the study area is larger than that in the east, especially in the Panzhihua, where the intensity of anisotropy is less than 2% and the direction becomes to ENE-WSW.

4. Discussion

4.1 Comparison with previous results

At short periods (8 ~ 10 s), we can see three distinct high-velocity zones in the northwestern, northeastern, and southern parts of the study area, respectively. The low-velocity zones are distributed beneath the LXF, RRF, CXF and TCV. The azimuthal anisotropy mainly aligns N-S direction. This distribution patterns of velocity and azimuthal anisotropy are consistent with previous results in the study area [Han et al., 2022; Pan et al., 2015; Qin et al., 2018; Wang and Gao., 2014; Wang et al., 2014; Wang et al., 2015; Yao et al., 2010; Zheng et al., 2014]. For example, the high-velocity zones in Weixi region are consistent with the phase velocity results obtained by Wang et al [2014] at period 10 s using the surface wave records of 504 teleseismic events at 50 temporary and 92 permanent seismic stations in southwest China. Geological data indicate that the Weixi region is located in Lanping-Simao fold belt, and the sediment stratum are mainly marine facies strata of Triassic, Cretaceous and Jurassic [Li et al., 2021]. Receiver function analysis has further suggested that the Weixi region possesses a thick crust and a high Poisson's ratio [Wang et al., 2017; Zhang and Gao et al., 2019], with intermittent exposure of ultramafic rocks in the north-south direction [Xu et al., 2021]. Therefore, the high-velocity anomaly in this region could be related to crustal thickness and ultramafic materials in the crust. Previous studies have also reported a southwestward extension of low-velocity zone from the LXF into TCV, with the azimuthal anisotropy in the low-velocity zone oriented in nearly N-S direction. However, our data have better coverage at the intersection of LXF and RRF (Figure 5), which can obtain high-resolution phase velocity and azimuthal anisotropy. The phase velocity maps at periods 5 s and 8 s show that the low-velocity zones of the LXF and the RRF are separated by a weak high-velocity zone in the Jianchuan region. At period 10 s, the low-velocity of Jianchuan region becomes more obvious, with the trend of the low-velocity zone aligning with the strikes of LXF and RRF. The azimuthal anisotropy in the low-velocity zone also varies from the nearly N-S direction at the northeast end of the LXF to ENE-WSW (8 s and 10 s) directions of the intersection area, and then to the nearly N-S and NNW-SSE direction in the RRF. As the period increase, the intensity of anisotropy increases in this low-velocity zone. From Figure 6b, we can see that the short periods phase velocity mainly reflects the upper crustal S wave velocity. Gao et al. [2019] used the local earthquakes recorded by SL-array to obtain the fast wave polarization directions of the intersection area of the two faults by S wave splitting, which is also ENE-WSW and nearly N-S directions. This consistency, on the one hand, shows the reliability of this results in this study, on the other hand, shows that the deformation of the intersection area is more complex.

At periods 12 ~ 20 s (Figure 9d ~ 9f), we find that the extent of the low-velocity zone gradually decreases, and the high-velocity zone on the south side of the RRF gradually increases correspondingly. The high- and low-velocity

anomalies in the study area are bounded by the RRF at period 20 s, with low-velocity on the northeast side and high-velocity on the southwest side. The same characteristics can also be observed in the phase velocity map at the periods 25 ~ 35 s, which is consistent with Wang et al. [2015] and Wang et al. [2014]. Receiver functions results show that the crust on west side of the RRF is thin and is thick on the east side [Figure 1b, Sun et al., 2012; Zhang and Gao, 2019; Wang et al., 2017; Zhu et al., 2021]. This pattern may imply the fault is divided by the thick crust (indicated by low-velocity anomalies) and the thin crust with shallow mantle (indicated by high-velocity anomalies). However, the azimuthal anisotropy maps at periods 12 ~ 35 s show a complex patterns, especially in the region between the LCJF and the RRF to the south 26°N, where the azimuthal anisotropy varies from the nearly N-S direction of the short periods to the NNW-SSE direction, and the intensity of anisotropy is also weaker than that of the short period. In addition, in the southern side of the LCJF, the azimuthal anisotropy varies from ENE-WSW to nearly N-S in the middle and then to NNW-SSE in the south, which is consistent with the strike of the fault, indicating that the anisotropy of the block is mainly related to the fault structure.

From periods 5 to 35 s, the Panzhihua region consistently exhibits a high-velocity, which is consistent with the phase velocity results of Wang et al. [2014] and Han et al. [2022]. Wang et al. [2014] speculated that the high-velocity in this region might be related to the evolution of the Yangtze platform. Importantly, this high-velocity zone corresponds exactly to the inner zone of the ELIP (pink dashed area in Figure 9). Numerous studies have suggested that the inner zone of ELIP is a rigid region characterized by high *VP*, high *VS*, high *VP*/*VS*, high density, low heat flow, high resistivity, weak azimuthal anisotropy and negative radial anisotropy in the crust [Chen et al., 2015; Deng et al., 2014; Hu et al., 2000; Jiang et al., 2018; Li et al., 2020; Liu et al., 2021; Wang et al., 2014; Xu et al., 2015]. Wu and Zhang [2012] also found a high-velocity body in the middle-lower crust of the inner zone of ELIP, which is considered to be the relic of Permian paleomantle plume action. Huang et al. [2021] suggested that the high-velocity body indicates the large-scale magmatic underplating and intraplating, which not only changed the crustal structure and composition of the Sichuan-Yunnan rhombic block, but also changed the crustal rheological strength. Zhang et al. [2020] suggested that the high-velocity zone may be related to the basal-hyperbasal material remaining in the crust during the formation of the ELIP. Based on the results and conclusions of previous studies, we suggest that the high-velocity zone in the Panzhihua region are mainly related to the ELIP.

The TCV region (24°40'-25°30'N, 98°15'-98°45'E) is located along the southeast edge of the collision zone between the Indian and Eurasian Plates, away from the eastern boundary of the Indian plate by about 300 km [Sun et al., 2016]. It is one of the youngest volcano groups in mainland China, comprising dozens of volcanoes, and has significant volcanic and thermal activity, as well as seismicity [Du et al., 2005; Li et al., 2018; Wang and Huang, 2004]. Previous studies have confirmed that TCV region exhibits characteristics such as high heat flow, low resistivity, high Poisson's ratio and low velocity, suggesting the presence of magma chambers and molten materials beneath the volcano [Bai et al., 2001; Hu et al., 2000; Lei et al., 2009; Li et al., 2016, 2018; Wang and Huang, 2004; Wang et al., 2017; Wu et al., 2016; Ye et al., 2018; Zhao et al., 2021]. Both the results of this study and previous results [Han et al., 2022; Pan et al., 2015; Qin et al., 2018; Wang et al., 2014; Wang et al., 2015; Wang et al., 2020] show that low phase velocity is present beneath the TCV. However, the shape of the low-velocity zone is still different from the results of the above results, especially at short period (Figure 9a ~ 9c). At periods 5 ~ 10 s, the low-velocity zones in the TCV and Shidian regions are separated by a weak high-velocity zone exhibiting a nearly N-S distribution. From 15 to 35 s, the low-velocity anomaly is mainly distributed in the north of TCV. The deep seismic sounding by Bai and Wang [2003] revealed the existence of a high-velocity body on the south side of the LRF. They suggested that the high-velocity body likely represents a block associated with the process of magma upwelling. Therefore, we suggest that the low-velocity beneath the TCV may be related to the magma chamber beneath the volcano area, while the high-velocity between TCV and Shidian region may reflect solidified magma intrusions and high-density remnants within the cooled volcanic channel prior to Pleistocene [Xu et al., 2012].

4.2 Anisotropy characteristics of each tectonic block in the Sanjiang lateral collision zone

Anisotropy refers to the variation of seismic wave propagation velocity with the direction in the medium [Crampin et al., 1980]. A large number of studies have shown that anisotropy exists in different depths of the earth, which is a common physical phenomenon in the interior of the earth [Crampin, 1978]. Seismic anisotropy is closely related to geological tectonic, deep material movement and stress-strain of medium. It is one of the effective means to study deformation of crust-mantle medium, material migration and dynamic evolution of lithosphere [Hirn et al.,

1995; Kong et al., 2016]. Studies have shown that the upper crust anisotropy is mainly caused by the directional arrangement of the EDA (extensive-Dilatancy Anisotropy) microcracks induced by regional stress [Crampin and Gao, 2014; Crampin and Peacock, 2008]. The middle-lower crust anisotropy may also be caused by dominant arrangement of minerals and melt lattices in rocks [Barruol and Mainprice, 1993]. Anisotropy in different depths of the earth can be obtained by using different types of seismic body wave or surface wave data. Therefore, it is of great significance to analyze the internal deformation, deep tectonic and dynamic model of the earth by combining various anisotropic data. In this paper, the azimuthal anisotropies at selected periods (8 s, 20 s, 35 s) are compared with fast polarization directions of S wave reflecting the anisotropy of the middle and upper crust [Gao et al., 2019; Shi et al., 2012; Tai et al., 2015; Zhang and Gao, 2017] and fast polarization directions of PmS wave reflecting the anisotropy of the whole crust [Cai et al., 2016; Peng et al., 2022; Sun et al., 2012; Sun et al., 2013] to analyze the crustal deformation characteristics in the study area. To facilitate discussion, the study area is divided into 5 subzones (Figure 10) based on major tectonic and the dividing line (purple shadow) of lithospheric anisotropy of lithosphere by Gao et al. [2020], including the subzone A (pink shadow area), subzone B (powder-blue shadow area), subzone C (yellow shadow area), subzone D (orange shadow area) and subzone E (light-blue shadow area). Here, we do not discuss the results of the S wave splitting in subzone A, due to the lack of data in previous studies in the region.

Overall, the directions of regional principal compressive stress obtained from the inversion of the focal mechanism solutions show clockwise rotation from north to south of the study area (Figure 10). The principal compressive stress directions are NNW-SSE and NW-SE in the WSB and CYB. The directions are NE-SW and nearly N-S in the TCB and the south of ICB, respectively. The surface velocity field measured by GPS data shows that, compared with the stable Eurasian plate, the crust in the study area rotates clockwise, showing NNW-SSE movement in the north, nearly N-S in the middle, and gradually NE-SW in the southwest [Figure 10a, Zhao et al., 2015]. This rotation pattern is consistent with the azimuthal anisotropies observed in the study area. The alignment of the azimuthal anisotropies with the directions of regional principal compressive stress and GPS velocity field suggests a close relationship between the crustal deformation, stress field, and anisotropic properties of the medium.

The subzone A is composed of the northern part of the TCB and the ICB. It is located in the edge of the convergence, subduction and interaction of the Eurasian and Indian plates. There are many NNW-SSE and nearly N-S trending faults. The collision between the Eurasian and Indian plates and the blocking of the Sichuan Basin, results in significant compression and the occurrence of numerous normal-fault earthquakes. The stress field is characterized by NNW-SSE compression and ENE-WSW tension [Tian et al., 2019], and the GPS velocity field is also NNW-SSE direction (Figure 10a). In this subzone, the fast velocity directions of 8 s, 20 s and 35 s show good consistency and vary from ENE-WSW to nearly N-S from west to east (Figure 10b ~ Figure 10d, Figure 11). The dominant direction is nearly N-S, which is consistent with the strikes of large-scale strike-slip faults. The fast wave directions of PmS waves beneath most stations are parallel to the faults, showing nearly N-S and NNW-SSE directions. There are two dominant directions, namely NNW-SSE and nearly E-W directions, but they are consistent with the fast velocity directions as a whole. We suggest that faults play a significant role in controlling the azimuthal anisotropy and crust deformation in this region. In addition, we observe that the intensity of azimuthal anisotropy is larger than that of other regions, indicating that the southeastward extrusion of the Tibetan plateau materials exerts a stronger influence in the region.

The subzone B is composed of the WSB and the northern part of the CYB. It is located in the Sichuan-Yunnan rhombic block, with NE-SW, NNW-SSE and nearly N-S trending faults, of which the LXF is an important fracture in the study area, dividing the Sichuan-Yunnan rhombic block into two north-south blocks, namely the WSB and the CYB [Xiang et al., 2002]. The study shows that the LXF absorbs part of the left-lateral strike-slip deformation transmitted from the Xianshuihe fault to the SE. The horizontal and vertical slip rates since the Quaternary are 3.7-3.8 mm/a and 0.6-1.5 mm/a, respectively [Xiang et al., 2002]. Figure 11 shows that the dominant fast velocity directions of periods 8 s, 20 s and 35 s have good consistency in near N-S, which is different from the fast wave dominant direction of S wave in near E-W direction and PmS wave in NNW-SSE direction (Figure 11). However, we found slight differences in anisotropy on both sides of LXF (Figure 10). In the north side of the fault, the FDs are NNW-SSE and near N-S, and the south side are ENE-WSW. The same characteristics can also be observed in the PmS wave splitting results. The fast wave direction of PmS wave is ENE-WSW on both sides of near the fault, but it is NW-SE on both sides away from the fault. In addition, the fast wave direction of S wave at stations near LXF is also ENE-WSW. These directions align with the strike of the LXF and suggest that the LXF, in particular, may have a strong influence on the anisotropy observed in this area. The presence of faults, such as the LXF and JQF, plays a significant role in shaping the seismic anisotropy within subzone B. The interaction and slip along these faults can

introduce variations in the propagation of seismic waves, leading to the observed anisotropy discrepancies between S wave and PmS wave. The local tectonic features and fault characteristics are crucial factors in determining the anisotropic patterns in this region.

In the subzone C, the fast velocity directions of period 8 s show nearly N-S and ENE-WSW (Figure 10b). The anisotropy intensity is relatively strong. At period 20 s, the fast velocity directions show NNW-SSE in the northwest part, which is consistent with the strike of the RRF, while in the southeast part, the directions are ENE-WSW, and the

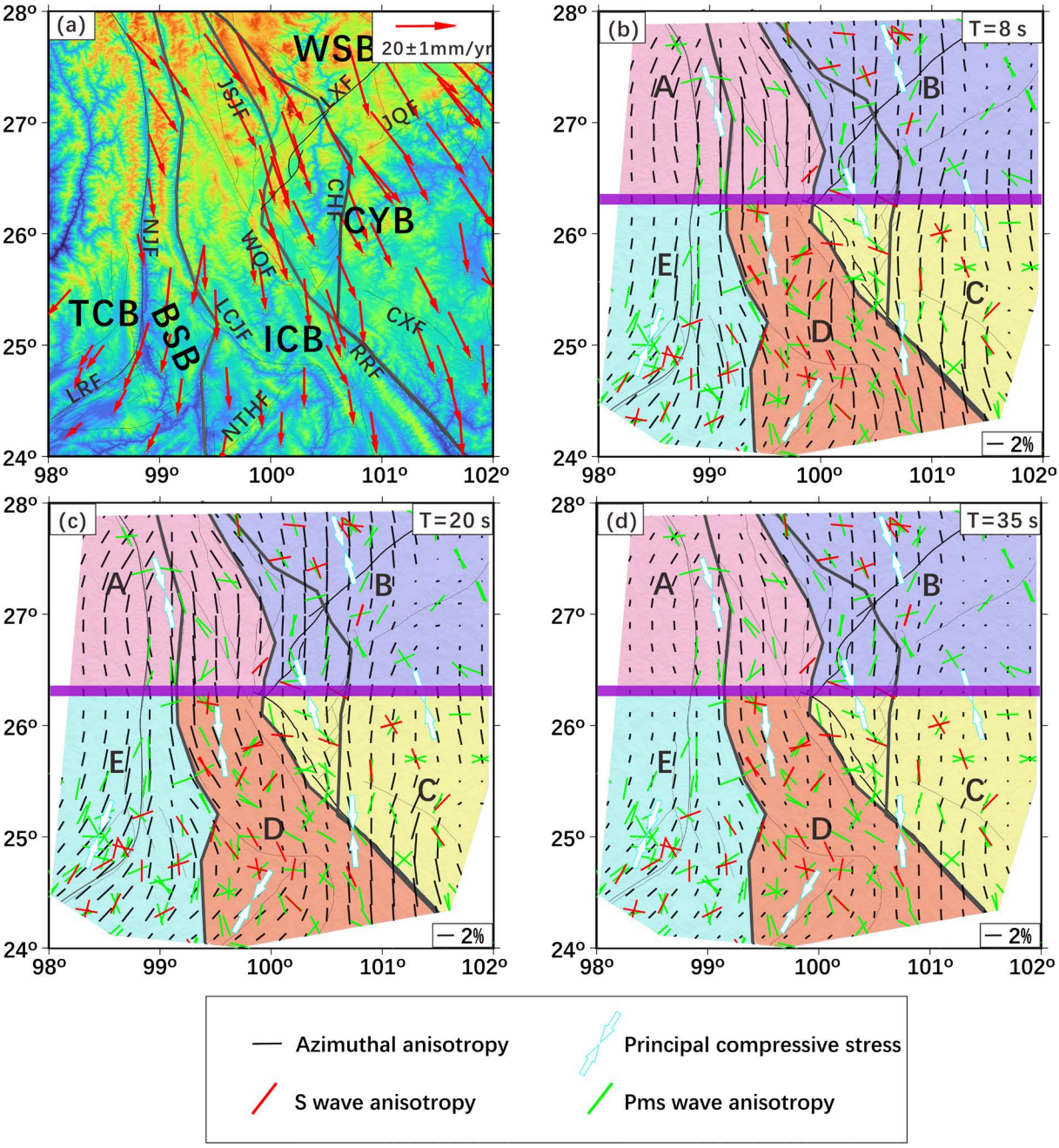

Figure 10. Comparison of anisotropy in the study area. (a) GPS velocity field of crust motion relative to the stable Eurasia plate [Zhao et al., 2015]. (b)-(d) The comparison of the Rayleigh wave azimuthal anisotropy (black lines) at periods 8 s, 20 s, 35 s with regional principal compressive stress [pair of arrows, Cui et al., 2006; Tian et al., 2019; Wu et al., 2004], S wave anisotropy [red lines, Gao et al., 2019; Shi et al., 2012; Tai et al., 2015; Zhang and Gao, 2017] and PmS wave anisotropy [green lines, Cai et al., 2016; Peng et al., 2022; Sun et al., 2012; Sun et al., 2013]. The letters A, B, C, D and E are five subzones in different colors. The purple shadow is dividing line of lithosphere anisotropy by Gao et al. [2020]. Other symbols and abbreviations are consistent with Figure 1.

intensity of anisotropy is still strong (Figure 10c). At period 35 s, the fast velocity directions are similar with those at period 20 s, although the intensity of anisotropy is weakened (Figure 10d). The dominant azimuthal anisotropy direction is NNW-SSE (Figure 11), which is distinct from the dominant direction (NWW-SEE) of S wave, but it has similarity with the dominant direction of PmS wave (Figure 11). The subzone is the south-central part of the Sichuan-Yunnan rhombic block bounded by the RRF. The GPS observations also reveal that the Sichuan-Yunnan rhombic block has the characteristics of clockwise rotation around the eastern Himalayan syntaxis. Due to the eastward extrusion of the Tibetan Plateau material, the region is subjected to NNW-SSE extrusion and ENE-WSW tensile stress structure [Cui et al., 2006; Tian et al., 2019; Wu et al., 2004]. As the western boundary of the Sichuan-Yunnan rhombic block, the RRF plays an important role in the southeastward extrusion of the material from the SE margin of the Tibetan Plateau. The azimuthal anisotropy of this study shows that the fast velocity direction of the short period (8 s) is N-S near the RRF, and the medium-long period (20 ~ 35 s) is NNW-SSE direction in line with the strike of the fault. The previous research results also show that after 30 s, the phase velocity azimuthal anisotropy is consistent with the strike of the RRF [Han et al., 2022]. Cai et al. [2016] suggested that the strike-slip movement of the faults in the Sichuan-Yunnan region caused the deformation of the crust and distribution of minerals and melts along the strike of the fault, resulting in an anisotropic fast wave direction parallel to the strike of the fault. Therefore, the anisotropy in this area may not only be related to the clockwise rotation of the southeastward extrusion of the plateau material, but also the RRF has a great influence on the crustal deformation in this area.

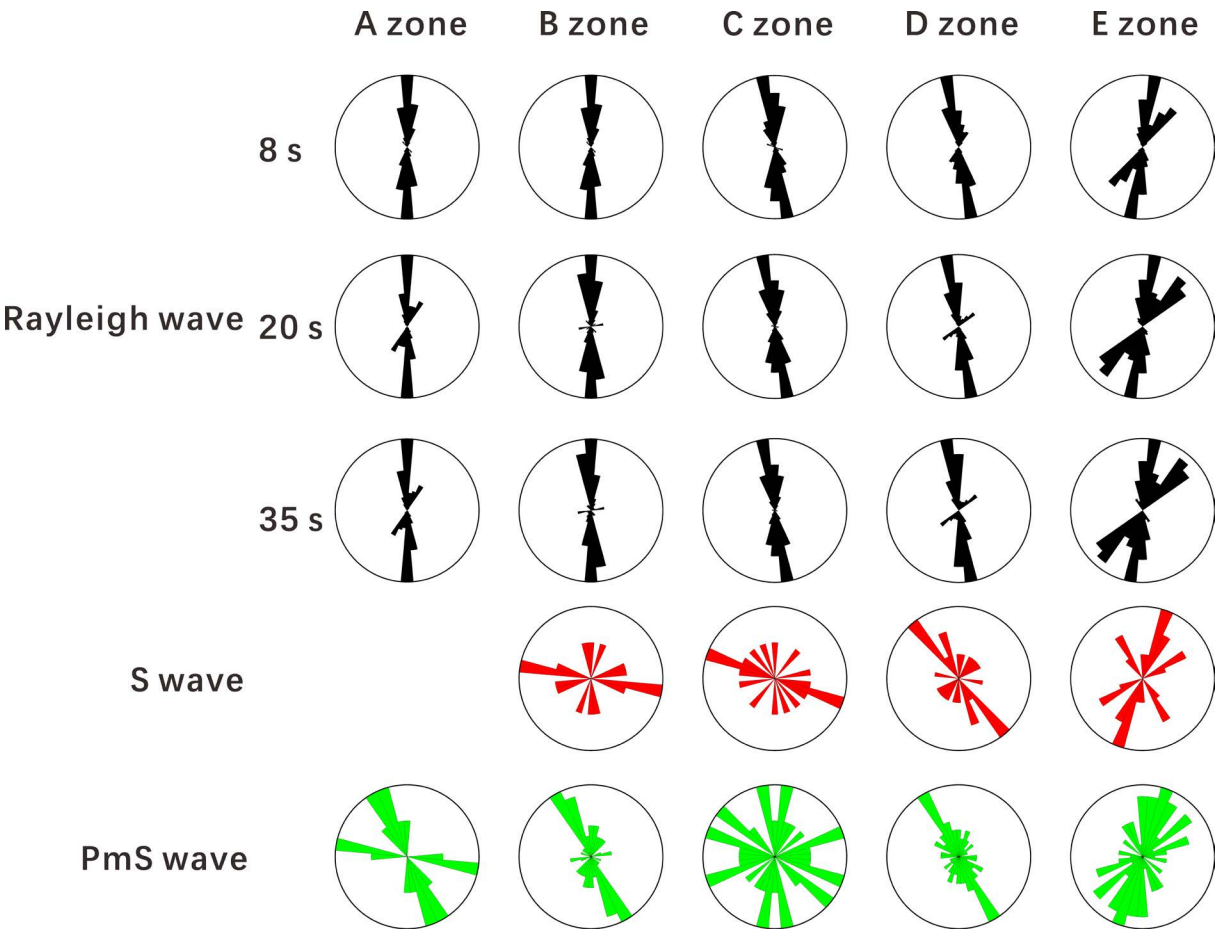

Figure 11. Fast polarizations at each subzone. Each circle plot is the equal-area project rose diagram of fast polarizations at each subzone. The letters above rose diagram are subzones codes, the letters in the left of rose diagram are the types of seismic waves. The black equal-area project rose diagram is Rayleigh wave azimuthal anisotropy, which is fast velocity directions of 8 s, 20 s, 35 s from top to bottom, the red equal-area project rose diagram is S wave fast polarizations, the green equal-area project rose diagram is PmS wave fast polarizations. The fast wave polarization data of S and PmS waves are consistent with Figure 10.

The subzone D is located in the southern part of the ICB. At period 8 s (Figure 10b), the fast velocity directions are nearly N-S in the north, NNW-SSE and ENE-WSW in the south, and the dominant direction is NNW-SSE (Figure 11). The anisotropy intensity is stronger in the south than that in the north. At period 20 s (Figure 10c), the fast velocity directions become NNW-SSE in the north, ENE-WSW and nearly N-S in the south, and the dominant direction is NNW-SSE (Figure 11), but the anisotropy intensity decreases in the south and is still strong in the north. The fast velocity directions of period 35 s are consistent with those of period 20 s, but the anisotropy intensity is weakened (Figure 10d). The tectonic stress field obtained by focal mechanism inversion also shows clockwise rotation from north to south. The azimuthal anisotropy in this region is basically consistent with the dominant directions of S and PmS waves (Figure 10 and Figure 11). We suggest that the azimuthal anisotropy at short period may be controlled by the regional stress field, while the anisotropy from 20 s to 35 s is mainly controlled by the RRF on the eastern boundary and the LCJF on the western boundary.

The subzone E is located in the southern part of the Yunnan-Myanmar-Thailand block. There are many ENE-WSW and NNW-SSE oriented faults. The fast velocity directions at periods 8 s, 20 s and 35 s display consistent patterns. The fast velocity directions rotate clockwise from east to west, from NNW-SSE to nearly N-S and then to ENE-WSW direction, which are consistent with the strikes of faults, GPS velocity field and maximum principal compressive directions in the region (Figure 10). The dominant direction is ENE-WSW and NE-SW direction, which are also consistent with the fast wave directions of S and PmS waves (Figure 11). We suggest that the azimuthal anisotropy in this region is affected by both fault tectonic and regional stress field. The intensity of anisotropy gradually increases from north to south, indicating the magmatism beneath TCV has caused strong deformation in this region.

5. Conclusions

In this study, we used ambient noise dispersion data from 176 seismic stations in the study area to obtain the high-resolution Rayleigh wave phase velocity and azimuthal anisotropy. Combined with the regional tectonic stress field, GPS data, S wave and PmS wave anisotropy, we obtained the following major conclusions.

1) At periods 5 ~ 8 s, the low-velocity anomalies are found beneath the LXF, RRF, CXF and TCV, the high-velocity anomalies are in the region of Weixi and Panzhihua. The distributions of high- and low-velocity are corresponding to the distribution of geological structure. At periods 10 ~ 15 s, the distributions of low-velocity anomalies are consistent with the strikes of LXF and RRF. At periods 20 ~ 35 s, the high- and low-velocity anomalies are bounded by the RRF, which may imply the fault is divided by the thick crust (indicated by low-velocity anomalies) and the thin crust with shallow mantle (indicated by high-velocity anomalies).
2) The direction and intensity of anisotropy shows significant variations. At periods 5 ~ 8 s, the fast velocity directions mainly align N-S in the study area. At periods 10 ~ 35 s, the fast velocity directions vary from N-S to NNW-SSE and then to ENE-WSW in a clockwise rotation from north to south of the study area, indicating that the deformation of the Sanjiang lateral collision zone is obviously affected by the deep fracture. The intensity of anisotropy in the low-velocity zone is stronger than that in the high-velocity zone, and the intensity in the north of the study area is stronger than that in the south.
3) By comparison, the fast velocity dominant directions are always nearly N-S in subzones A and B, subzones C and D are NNW-SSE directions, the subzone E is ENE-WSW or NE-SW directions as the period increases. The fast velocity directions of other subzones are basically consistent with the fast wave directions of S wave, except for subzones B and C. The fast velocity directions of all subzones are basically consistent with the fast wave directions of PmS wave.

Acknowledgements. We appreciate three anonymous reviewers and editors for their constructive comments and suggestions. We acknowledge the data center of Institute of Earthquake Forecasting, China Earthquake Administration and the data center of China Earthquake Discipline of Institute of Geophysics, China Earthquake Administration for providing continuous waveform data of temporary seismic arrays. We acknowledge Prof. Huajian Yao and Dr. Chuanming Liu for providing ambient noise calculation program. This paper is supported by National Natural Science Foundation of China (Project 41730212), National Key R&D Project of China (2017YFC1500304) and Central Public-interest Scientific Institution Basal Research Fund (No. 2021IEF0103). The GMT drawing software was used for drawing the graphics in this study.

References

Bai, D. H., M. A. Meju, and Z. J. Liao (2001). Magnetotelluric images of deep crustal structure of the Rehai geothermal field near Tengchong, southern China, Geophys. J. Int., 147, 3, 677-687.

Bai, D. H., M. J. Unsworth, M. A. Meju, X. B. Ma, J. W. Teng, X. R. Kong, Y. Sun, J. Sun, L. F. Wang, C. S. Jiang, C. P. Zhao, P. F. Xiao, and M. Liu (2010). Crustal deformation of the eastern Tibetan Plateau revealed by magnetotelluric imaging, Nat. Geosci., 3, 5, 358-362.

Bai, Z. M., and C. Y. Wang (2003). Tomographic investigation of the upper crustal structure and seismotectonic environments in Yunnan province, Acta Seismol. Sin. (in Chinese),16, 2, 127-139.

Bao, X. W., X. X. Sun, M. J. Xu, D. W. Eatond, X. D. Song, L. S. Liu, Z. F. Ding, N. Mi, H. Li, D. Y. Yu, Z. C. Huang, and P. Wang (2015). Two crustal low-velocity channels beneath SE Tibet revealed by joint inversion of Rayleigh wave dispersion and receiver functions, Earth Planet. Sci. Lett., 415,16-24.

Barruol, G., and D. Mainprice (1993). A quantitative evaluation of the contribution of crustal rocks to the shear-wave splitting of teleseismic SKS waves, Phys. Earth Planet. Inter., 78, 3-4, 281-300.

Bensen, G. D., M. H. Ritzwoller, M. P. Barmin, A. L. Levshin, F. Lin, M. P. Moschetti, N. M. Shapiro, Y. Yang (2007). Processing seismic ambient noise data to obtain reliable broad-band surface wave dispersion measurements, Geophys. J. Int., 169, 3, 1239-1260.

Cai, Y, J. P. Wu, L. H. Fang, W. L. Wang, and Y. Shuang (2016). Crustal anisotropy and deformation of the southeastern margin of the Tibetan Plateau revealed by Pms splitting, J. Asia Earth Sci., 121,120-126.

Chang, L. J., Z. F. Ding, and C. Y. Wang (2015). Upper mantle anisotropy beneath the southern segment of North-South tectonic belt, Chinese J. Geophys. (in Chinese), 58, 11, 4052-4067.

Chen, H. P., L. B. Zhu, and Y. J. Su (2016). Low velocity crustal flow and crust-mantle coupling mechanism in Yunnan, SE Tibet, revealed by 3D S-wave velocity and azimuthal anisotropy, Tectonophysics, 685, 8-20.

Chen, M., H. Huang, H. J. Yao, R. D. van der Hilst, and F. L. Niu (2014). Low wave speed zones in the crust beneath SE Tibet revealed by ambient noise adjoint tomography, Geophys. Res. Lett., 41, 334-340.

Chen, Y., Y. G. Xu, T. Xu, S. K. Si, X. B. Liang, X. B. Tian, Y. F. Deng, L. Chen, P. Wang, Y. H. Xu, H. Q. Lan, F. H. Xiao, W. Li, X. Zhang, X. H. Yuan, J. Badal, and J. W. Teng (2015). Magmatic underplating and crustal growth in the Emeishan Large Igneous Province, SW China, revealed by a passive seismic experiment, Earth Planet. Sci. Lett., 432, 103-114.

Crampin, S (1978). Seismic-wave propagation through a cracked solid: polarization as a possible dilatancy diagnostic, Geophys. J. Int., 53, 3, 467-496.

Crampin, S., and S. Peacock (2008). A review of the current understanding of seismic shear-wave splitting in the Earth's crust and common fallacies in interpretation, Wave Motion, 45, 6, 675-722.

Crampin, S., and Y. Gao (2014). Two species of microcracks, Appl. Geophys., 11, 1, 1-8.

Crampin, S., R. McGonigle, and D. Bamford (1980). Estimating crack parameters from observations of P wave velocity anisotropy, Geophysics, 45, 3, 345-360.

Cui, X. F., F. R. Xie, and H. Y. Zhang (2006). Recent tectonic stress field zoning in Sichuan Yunnan region and its dynamic interest, Acta Seismol. Sin., 19, 5, 485-496.

Deng, Y. F., Z. J. Zhang, W. Mooney, J. Badal, W. M. Fan, and Q. Zhong (2014). Mantle origin of the Emeishan large igneous province (South China) from the analysis of residual gravity anomalies, Lithos, 204, 4-13.

Du, J. G., C. Q. Liu, B. H. Fu, Y. Ninomiya, Y. L. Zhang, C. Y. Wang, H. L. Wang, and Z. G. Sun (2005) Variations of geothermometry and chemical-isotopic compositions of hot spring fluids in the Rehai geothermal field, southwestern China, J. Volcanol. Geotherm. Res., 142, 3-4, 243-261.

Fang, H. J., H. J. Yao, H. J. Zhang, Y. C. Huang, and R. D. var der Hilst (2015). Direct inversion of surface wave dispersion for three-dimensional shallow crustal structure based on ray tracing: methodology and application, Geophys. J. Int., 201, 3, 1251-1263.

Gao, Y., A. G. Chen, Y. T. Shi, Z. Q. Zhang, and L. B. Liu (2019). Preliminary analysis of crustal shear-wave splitting in the Sanjiang lateral collision zone of the southeast margin of the Tibetan Plateau and its tectonic implications, Geophys. Prospect., 67, 9, 2432-2449.

Gao, Y., and J. Wu (2008). Compressive stress field in the crust deduced from shear-wave anisotropy: an example in capital area of China, Chinese Sci. Bull., 53, 18 2840-2848.

Gao, Y., J. Wu, Y. Fukao, Y. T. Shi, and A. L. Zhu (2011). Shear wave splitting in the crust in North China: stress, faults and tectonic implications, Geophys. J. Int., 187, 2, 642-654.

Gao, Y., Y. T. Shi, and Q. Wang (2020). Seismic anisotropy in the southeastern margin of the Tibetan Plateau and its deep tectonic significance, Chinese J. Geophys. (in Chinese), 63, 3, 802-816.

Han, C. R., Z. C. Huang, S. J. Hao, L. S. Wang, M. J. Xu, and J. O. S. Hammond (2022). Restricted lithospheric extrusion in the SE Tibetan Plateau: Evidence from anisotropic Rayleigh-wave tomography, Earth Planet. Sci. Lett., 598, 117837.

Hirn, A., M. Jiang, M. Sapin, J. Diaz, A. Nercessian, Q. T. Lu, J. C. Lépine, D. N. Shi, M. Sachpazi, M. R. Pandey, K. Ma, and J. Gallart (1995). Seismic anisotropy as an indicator of mantle flow beneath the Himalayas, Nature, 375, 6532, 571-574.

Hu, S., L. He, and J. Wang (2000). Heat flow in the continental area of China: a new data set, Earth Planet. Sci. Lett., 179, 407-419.

Huang, Z. C., C. Ji, H. T. Wu, Y. T. Shi, J. Q. Geng, M. J. Xu, C. R. Han, M. J. Xu, and L. S. Wang (2021). Review on the crustal structures and deformations in the southeastern margin of the Tibetan Plateau, Rev. Geophys. Planet. Phys. (in Chinese), 52, 3, 291-307.

Jiang, Q., N. S. Qiu, and C. Q. Zhu (2018). Heat flow study of the Emeishan large igneous province region: Implications for the geodynamics of the Emeishan mantle plume, Tectonophysics, 724-725, 11-27.

Jin, H. L., Y. Gao, X. N. Su, and G. Y. Fu (2019). Contemporary crustal tectonic movement in the southern Sichuan-Yunnan block based on dense GPS observation data, Earth Planet. Phys., 3, 1, 55-63.

Kong, F. S., J. Wu, K. H. Liu, and S. S. Gao (2016). Crustal anisotropy and ductile flow beneath the eastern Tibetan Plateau and adjacent areas, Earth Planet. Sci. Lett., 442, 72-79.

Lei, J. S., D. P. Zhao, and Y. J. Su (2009). Insight into the origin of the Tengchong intraplate volcano and seismotectonics in southwest China from local and teleseismic data, J. Geophys. Res., 114, B05303, 1-18.

Lei, J. S., Y. Li, F. R. Xie, J. W. Teng, G. W. Zhang, C. Q. Sun, and X. H. Zha (2014). Pn anisotropic tomography and dynamics under eastern Tibetan plateau, J. Geophys. Res. Solid Earth, 119, 2174-2198.

Lev, E., M. D. Long, and R. D. van der Hilst (2006). Seismic anisotropy in Eastern Tibet from shear wave splitting reveals changes in lithospheric deformation, Earth Planet. Sci. Lett., 251, 3-4, 293-304.

Li, D. H., Z. F. Ding, P. P. Wu, S. Liu, F. Deng, X. Zhang, and H. Zhao (2021).The characteristics of crustal structure and seismogenic background of Yangbi *M*S6.4 earthquake on May 21, 2021 in Yunnan Province, China, Chinese J. Geophys. (in Chinese), 64, 9, 3083-3100.

Li, M. K., S. X. Zhang, F. Wang, T. F. Wu, and W. B. Qin (2016). Crustal and uppermantle structure of the southeastern Tibetan Plateau from joint analysis of surface wave dispersion and receiver functions, J. Asia Earth Sci., 117, 52-63.

Li, M. K., S. X. Zhang, T. F. Wu, Y. J. Hua, and B. Zhang (2018). Fine crustal and uppermost mantle S-wave velocity structure beneath the Tengchong volcanic area inferred from receiver function and surface-wave dispersion: constraints on magma chamber distribution, Bull. Volcanol., 80, 25.

Li, X., X. B. Ma, Y. Chen, S. Xue, I. M. Varentsov, and D. H. Bai (2020). A plume-modified lithospheric barrier to the southeastward flow of partially molten Tibetan crust inferred from magnetotelluric data, Earth Planet. Sci. Lett., 548, 116493.

Liu, C. M., H. J. Yao, H. Y. Yang, W. S. Shen, H. J. Fang, S. Q. Hu, and L. Qiao (2019). Direct inversion for three-dimensional shear wave speed azimuthal anisotropy based on surface wave ray tracing: Methodology and application to Yunnan, southwest China, J. Geophys. Res. Solid Earth, 124, 11394-11413.

Liu, Y. D., L. Li, J. van Wijk, A. B. Li, and Y. Y. V. Fu (2021). Surface-wave tomography of the Emeishan large igneous province (China): Magma storage system, hidden hotspot track, and its impact on the Capitanian mass extinction, Geology, 49, 9, 1032-1037.

Li, Y. H., J. T. Pan, Q. J. Wu, and Z. F. Ding (2014). Crustal and uppermost mantle structure of SE Tibetan plateau from Rayleigh-wave group-velocity measurements, Earthq. Sci., 27, 4, 411-419.

Liu, Z. Q., X. Z. Li, and Q. T. Ye (1993). Delineation of tectonic magmatic zones and mineral distribution patterns in the Sanjiang region, Geological Press (in Chinese), Beijing, China.

Luo, S., H. J. Yao, Q. S. Li, W. T. Wang, K. S. Wan, Y. F. Meng, and B. Liu (2019). High-resolution 3D crustal S-wave velocity structure of the Middle-Lower Yangtze River Metallogenic Belt and implications for its deep geodynamic setting, Sci. China Earth Sci., 62, 9, 1361-1378.

Pan, J. T., Y. H. Li, Q. J. Wu, and Z. F. Ding (2015). Phase velocity maps of Rayleigh waves in the southeast Tibetan plateau, Chinese J. Geophys. (in Chinese), 58, 11, 3993-4006.

Pan, Y. S. (1991). Geotectonic evolution of the northwestern Tibet Plateau. Open research laboratory of lithospheric tectonic evolution, Institute of Geology, Chinese Academy of Sciences, 1989-1990, China Science and Technology Press (in Chinese), Beijing, China.

Peng, H. C., Z. H. Gao, J. F. Hu, H. Y. Yang, J. Badal, M. X. Chen, and T. J. Zhang (2022). Upper mantle anisotropy in the southeastern margin of the Tibetan plateau and geodynamic implications, Phys. Earth Planet. Inter., 327, 106877.

Qiao, L., H. J. Yao, Y. C. Lai, B. S. Huang, and P. Zhang (2018). Crustal structure of southwest China and northern Vietnam from ambient noise tomography: Implication for the large-scale material transport model in SE Tibet, Tectonics, 37, 1492-1506.

Qin, W. B., S. X. Zhang, M. K. Li, T. F. Wu, and C. Y. Zhang (2018). Distribution of intra-crustal low velocity zones beneath Yunnan from seismic ambient noise tomography, J. Earth Sci., 29, 1409-1418.

Rawlinson, N., and M. Sambridge (2004). Wave front evolution in strongly heterogeneous layered media using the fast marching method, Geophys. J. Int., 156, 3, 631-647.

Rawlinson, N., and M. Sambridge (2005). The fast marching method: an effective tool for tomographic imaging and tracking multiple phases in complex layered media, Explor. Geophys., 36, 4, 341-350.

Royden, L. H., B. C. Burchfiel, R. W. King, E. Wang, Z. L. Chen, F. Shen, and Y. P. Liu (1997). Surface deformation and lower crustal flow in eastern Tibet, Science, 276, 5313, 788-790.

Royden, L. H., B. C. Burchfiel, and R. D. van der Hilst (2008). The geological evolution of the Tibetan Plateau, Science, 321, 5892, 1054-1058.

Shi, Y. T., Y. Gao, Y. J. Su, and Q. Wang (2012). Shear-wave splitting beneath Yunnan area of southwest China, Earthq. Sci., 25, 1, 25-34.

Sun, C. Q., J. S. Lei, C. Li, G. W. Zhang, X. H. Zha, and F. Li (2013). Crustal anisotropy beneath the Yunnan region and dynamic implications, Chinese J. Geophys. (in Chinese), 56, 12, 4095-4105.

Sun, Y. J., Z. H. Wu, P. S. Ye, H. Zhang, H. L. Li, and Y. B. Tong (2016). Dynamics of the Tengchong volcanic region in the southeastern Tibetan plateau: a numerical study, Tectonophysics, 683, 272-285.

Sun, Y., F. L. Niu, H. F. Liu, Y. L. Chen, and J. X. Liu (2012). Crustal structure and deformation of the SE Tibetan plateau revealed by receiver functions data, Earth Planet. Sci. Lett., 349-350,186-197.

Tai, L. X., Y. Gao, G. Liu, and Z. Xiao (2015). Crustal seismic anisotropy in the southeastern margin of Tibetan Plateau by ChinArray data: shear-wave splitting from temporary observations of the first phase, Chinese J. Geophys. (in Chinese), 58, 11, 4079-4091.

Tian, J. H., Y. Luo, and L. Zhao (2019). Regional stress field in Yunnan revealed by the focal mechanisms of moderate and small earthquakes, Earth Planet. Phys., 3, 2, 1-10.

Wang, C. Y., and F. G. Huang (2004). Crustal structure in Tengchong volcano-geothermal area, western Yunnan, China, Tectonophysics, 380, 1, 69-87.

Wang, C. Y., H. Lou, P. G. Silver, L. P. Zhu, and L. J. Chang (2010). Crustal structure variation along 30°N in the eastern Tibetan and its tectonic implications, Earth Planet. Sci. Lett., 289, 3-4, 367-376.

Wang, C. Y., L. J. Chang, Z. Y. Lü, J. Z. Qin, W. Su, P. Silver and L. Flesch (2007). Seismic anisotropy of upper mantle in eastern Tibetan Plateau and related crust-mantle coupling patterns, Sci. China, Ser. D-Earth Sci., 50, 8, 1150-1160.

Wang, H. F., J. P. Wu, S. Y. Zhou, L. H. Fang, W. L. Wang, and Y. N. Liu (2020). Rayleigh wave azimuthal anisotropy in the Southeastern Tibetan Plateau from Eikonal tomography, Chinese J. Geophys. (in Chinese), 63, 3, 1070-1084.

Wang, M., and Z. K. Shen (2020). Present-day crustal deformation of continental China derivated from GPS and its tectonic implications, J. Geophys. Res. Solid Earth, 125, 2, e2019JB018774.

Wang, Q., and Y. Gao (2014). Rayleigh wave phase velocity tomography and strong earthquake activity on the southeastern front of the Tibetan Plateau, Sci. China Earth Sci., 57(10), 2532-2542.

Wang, Q., Y. Gao, and Y. T. Shi (2015). Rayleigh wave azimuthal anisotropy on the southeastern front of the Tibetan Plateau from seismic ambient noise, Chinese J. Geophys. (in Chinese), 58, 11, 4068-4078.

Wang, W. L., J. P. Wu, L. H. Fang, G. J. Lai, T. Yang, and Y. Cai (2014). S-wave velocity structure in southwest China from surface wave tomography and receiver functions, J. Geophys. Res. Solid Earth, 119, 2, 1061-1078.

Wang, W. L., J. P. Wu, L. H. Fang, G. J. Lai, and Y. Cai (2017). Crustal thickness and Poisson's ratio in southwest China based on data from dense seismic arrays, J. Geophys. Res. Solid Earth, 122, 9, 7219-7235.

Wu, J. P., Y. H. Ming, and C. Y. Wang (2004). Source mechanism of small-moderate earthquakes and tectonic stress field in Yunnan province, Acta Seismol. Sin., 17, 5, 509-517.

Wu, J., and Z. J. Zhang (2012). Spatial distribution of seismic layer, crustal thickness, and *Vp*/*Vs* ratio in the Permian Emeishan Mantle Plume region, Gondwana Res., 22, 1, 127-139.

Wu, T. F., S. X. Zhang, M. K. Li, W. B. Qin, and C. Y. Zhang (2016). Two crustal flowing channels and volcanic magma migration underneath the SE margin of the Tibetan Plateau as revealed by surface wave tomography, J. Asia Earth Sci., 132, 25-39.

Wu, T. F., S. X. Zhang, M. K. Li, M. Hong, and Y. J. Hua (2019). Complex deformation within the crust and upper mantle beneath SE Tibet revealed by anisotropic Rayleigh wave tomography, Phys. Earth Planet. Inter., 286, 165-178.

Xiang, H. F., X. W. Xu, S. M. Guo, W. X. Zhang, H. W. Li, and G. H. Yu (2002). Sinistral thrusting along the Lijing-Xiaojinhe fault since quaternary and its geologic-tectonic significance-Shielding effect of transverse structure of intracontinental active block, Seismology and Geology (in Chinese), 24, 2, 188-198.

Xu, T., Z. J. Zhang, B. F. Liu, Y. Chen, M. H. Zhang, X. B. Tian, Y. G. Xu, and J. W. Teng (2015). Crustal velocity structure in the Emeishan large igneous province and evidence of the Permian mantle plume activity, Sci. China, Earth Sci., 58, 7, 1133-1147.

Xu, W., F. L. Liu, L. Ji, F. Wang, W. T. Xu, and D. Wang (2021). Middle Permian-Late Triassic magmatism in the Deqen-Weixi area of the Sanjiang Orogenic Belt: Implications for Paleo-tethyan evolution, Acta Petrologica Sin. (in Chinese), 37, 2, 462-480.

Xu, Y. G., B. He, S. L. Chung, M. A. Menzies, and F. A. Frey (2004). Geologic, geochemical, and geophysical consequences of plume involvement in the Emeishan flood-basalt province, Geology, 32, 10, 917-920.

Xu, Y., X. T. Yang, Z. W. Li, and J. H. Liu (2012). Seismic structure of the Tengchong volcanic area southwest China from local earthquake tomography, J. Volcanol. Geoth. Res., 239-240, 83-91.

Yang, T., J. P. Wu, L. H. Fang, and W. L. Wang (2014). Complex structure beneath the Southeastern Tibetan Plateau from teleseismic P-wave tomography, Bull. Seismol. Soc. Am., 104, 3, 1056-1069.

Yao, H. J., R. D. van der Hilst, and M. V. de Hoop (2006). Surface-wave array tomography in SE Tibet from ambient seismic noise and two-station analysis-I. Phase velocity maps, Geophys. J. Int., 166, 2, 732-744.

Yao, H. J., C. Beghein, and R. D. van der Hilst (2008). Surface wave array tomography in SE Tibet from ambient seismic noise and two-station analysis-II. Crustal and upper-mantle structure, Geophys. J. Int., 173, 205-219.

Yao, H. J., R. D. van der Hilst, and J. P. Montagner (2010). Heterogeneity and anisotropy of the lithosphere of SE Tibet from surface wave array tomography, J. Geophys. Res. Solid Earth, 115, B12, B12307.

Yao, H. J., S. Luo, C. Li, S. Q. Hu, and H. J. Fang (2023). Direct surface wave tomography for three dimensional structure based on surface wave traveltimes: Methodology review and applications, Rev. Geophys. Planet. Phys. (in Chinese), 54, 3, 231-251.

Ye, T., Q. H. Huang, X. B. Chen, H. Q. Zhang, Y. J. Chen, L. Zhao, and Y. Zhang (2018). Magma chamber and crustal channel flow structures in the Tengchong volcano area from 3D MT inversion at the intracontinental block boundary southeast of the Tibetan Plateau, J. Geophys. Res. Solid Earth, 123, 12, 11112-11126.

Yin, A., and T. M. Harrison (2000). Geologic evolution of the Himalayan-Tibetan orogen, Annu. Rev. Earth Planet. Sci., 28, 1, 211-280.

Zhang, Y., and Y. Gao (2017). The characteristics of crustal shear-wave splitting in North-South seismic zone revealed by near field recordings of two observation periods of ChinArray, Chinese J. Geophys. (in Chinese), 60, 6, 2181-2199.

Zhang, Z, Q., H. J. Yao, W. T. Wang, and C. M. Liu (2022). 3D Crustal azimuthal anisotropy reveals multi-stage deformation processes of the Sichuan Basin and its adjacent area, SW China, J. Geophys. Res. Solid Earth, 127, 1, e2021JB023289.

Zhang, Z. Q., and Y. Gao (2019). Crustal thickness and Poisson's ratios beneath the Chuxiong-Simao Basin in the Southeast Margin of the Tibetan Plateau, Earth Planet. Phys., 3, 1, 69-84.

Zhang, Z. Q., H. J. Yao, and Y. Yang (2020). Shear wave velocity structure of the crust and upper mantle in Southeastern Tibet and its geodynamic implications, Sci. China Earth Sci., 63, 9, 1278-1293.

Zhao, B., Y. Huang, C. H. Zhang, W. Wang, K. Tan, and, R. L. Du (2015). Crustal deformation on the Chinese mainland during 1998-2014 based on GPS data, Geod. Geodyn., 6, 1, 7-15.

Zhao, L. F., X. B. Xie, J. K. He, X. B. Tian, and Z. X. Yao (2013). Crustal flow pattern beneath the Tibetan Plateau constrained by regional Lg-wave Q tomography, Earth Planet. Sci. Lett., 383, 113-122.

Zhao, Y., Z. Guo, K. Wang, and Y. J. Yang (2021). A large magma reservoir beneath the Tengchong volcano revealed by ambient noise adjoint tomography, J. Geophys. Res. Solid Earth, 126, 7, e2021JB022116.

Zheng, D. C., Z. X. Ge, R. H. Yang, Z. X. Min, Y. C. Tang, M. M. Jiang, and W. D. Pang (2014). Broadband ambient noise tomography in Yunnan Province, Acta Seismol. Sin. (in Chinese), 36, 4, 602-614.

Zhong, D. L., and L. Ding (1993). Discussion of the Gondwana continental dispersion and Asian continental accretion, Asian accretion from the evolution of the Tethys in the Sanjiang and adjacent areas, Earthquake Press (in Chinese), Beijing, China, 5-8.

Zhu, Z. J., X. B. Wang, Z. Q. Liu, and C. T. Liang (2021). Seismic anisotropy in the southeastern margin of the Tibetan Plateau revealed by ambient noise tomography based on high-density array, Chinese J. Geophys. (in Chinese), 64, 3, 823-837.

***CORRESPONDING AUTHOR: Yuan GAO**,
Key Laboratory of Earthquake Prediction, Institute of Earthquake Forecasting, China Earthquake Administration, Beijing 100036, China
e-mail: qzgyseis@163.com; gaoyuan@cea-ies.ac.cn